Materials Research. 2026; 29: e20250713
DOI: https://doi.org/10.1590/1980-5373-MR-2025-0713

Effect of Solution Heat-treatment and Aging on the Corrosion Behavior and Microstructure of Biodegradable Mg–Y–Gd–Zr alloys

Franz Miller Branco Ferraz[a], *Bruno Xavier de Freitas*[b], *Paula Letícia Corrêa de Toledo Cury*[a], *Viviane Lima Freitas da Silva*[a], *Carlos Ângelo Nunes*[a], *Célia Regina Tomachuk*[a]*

[a]*Universidade de São Paulo, Escola de Engenharia de Lorena, Estrada Municipal do Campinho, 100, 12602-810, Lorena, SP, Brasil.*
[b]*Universidade Federal de Itajubá, Instituto de Engenharia Mecânica, Av. BPS, 1303, 37500-903, Itajubá, MG, Brasil.*

Received: November 10, 2025; Revised: March 15, 2026; Accepted: April 08, 2026

The influence of solution and aging heat-treatments on the corrosion behavior of a biodegradable Mg–Y–Gd–Zr alloy was investigated. Electrochemical behavior was assessed by potentiodynamic polarization curves and electrochemical impedance spectroscopy in an aerated 0.9 wt.% NaCl solution at 37 °C ± 0.1, complemented by SEM, EDS, and XRD analyses of corrosion-products. The as-cast condition exhibited the highest polarization resistance and impedance modulus, attributed to a thicker and more resistive corrosion-product layer, despite microstructural heterogeneity. Solution heat-treatment (525 °C/24 h) homogenized the microstructure and shifted the corrosion potential to nobler values, but produced a thinner, less protective film and reduced corrosion resistance. Among aged conditions, aging at 250 °C for 100 h yielded the best performance, with higher polarization resistance and impedance modulus values indicative of a more uniform and stable surface layer. Overall, the results demonstrate that corrosion behavior is primarily governed by the stability and resistive character of the corrosion-product layer, which is strongly controlled by the heat-treatment-induced microstructural state.

Keywords: *Biodegradable magnesium, Rare-earth elements, Magnesium-based alloy.*

1 Introduction

Magnesium and its alloys have attracted considerable attention as bioresorbable implant materials due to their unique combination of properties, including biocompatibility, biodegradability, and anti-inflammatory, antitumor, and antibacterial effects[1-3]. Unlike traditional permanent implant materials, magnesium alloys exhibit low density (1.4–2.0 g/cm^3) and an elastic modulus (41–45 GPa) that closely match those of cortical human bone, making them particularly suitable for temporary orthopedic applications[4,5]. However, pure magnesium presents critical limitations in physiological environments, including rapid degradation in chloride-rich media (pH 7.4–7.6). This degradation compromises mechanical integrity and releases hydrogen gas into the bloodstream, potentially leading to medical complications[6,7]. Overall, the degradation of Mg alloys is strongly influenced by their low standard electrode potential and high chemical activity, which make them highly susceptible to galvanic corrosion in physiological conditions. Moreover, the corrosion layer formed in such environments is generally soluble and poorly protective, resulting in porous structures upon exposure to chloride ions[8].

To overcome these challenges, alloying magnesium with rare earth elements (REEs) has been widely investigated as a strategy to enhance both corrosion resistance and mechanical performance[2,9,10]. In general, REEs have standard electrode potentials (SHE) that are comparable to or lower than that of Mg (−2.37 V), such as Y (−2.47 V), Gd (−2.27 V), and Nd (−2.32 V). As a result, REE-based phases typically exhibit low potentials and cathodic behavior[8]. Among these, gadolinium (Gd) is particularly effective: its high solubility in the Mg matrix (23.5 wt.%) promotes both solid-solution strengthening and age-hardening. When Gd atoms substitute for Mg atoms in the lattice, the induced lattice strain hinders dislocation motion, thereby improving yield strength[11]. However, the Mg_5Gd phase is more electrochemically noble than the Mg matrix, which can accelerate localized galvanic corrosion. This undesired effect can be mitigated by limiting Gd content to below 10 wt.%, ensuring partial dissolution of the phase back into the matrix[7].

Yttrium (Y) is also an effective alloying element due to its electrochemical potential being close to that of Mg and its hexagonal close-packed (HCP) crystal structure, which allows for high solubility in the Mg matrix and promotes significant grain refinement[7]. According to the Mg–Y phase diagram, Mg can dissolve up to 4 wt.% Y at 200 °C and up to 6 wt.% at 300 °C[12]. Zhang et al.[13] demonstrated that Y addition leads to grain refinement, while the $Mg_{24}Y_5$ phase effectively reduces corrosion rates in chloride-containing solutions. Liang et al.[14] further reported that Y addition enhances the corrosion resistance of Mg alloys by forming an effective barrier against grain-boundary corrosion initiation.

*e-mail: celiatomachuk@usp.br
Associate Editor: José Daniel Biasoli de Mello.
Editor-in-Chief: Luiz Antonio Pessan.

Specifically, Y decreases the number of intragranular precipitates while promoting their segregation along grain boundaries, thereby providing greater protection.

In addition to the improvements in corrosion behavior and mechanical properties, the use of REEs in magnesium alloys has been extensively evaluated from a biomedical perspective. Several in vitro and in vivo studies[15-18] have demonstrated that alloying Mg with REEs does not compromise its biocompatibility when these elements are added in controlled concentrations. Rare-earth elements such as Y, Gd, and Nd have been reported to exhibit acceptable biocompatibility, and the low ion release during degradation of Mg–REE alloys remains within non-toxic limits. These elements contribute to improved corrosion control and mechanical stability, which are critical for safe performance of biodegradable Mg-based implants[19-22].

Zirconium (Zr) is commonly employed as a grain refiner in magnesium alloys. Despite its limited solubility in pure Mg, undissolved Zr particles act as effective heterogeneous nucleation sites during solidification, resulting in fine equiaxed grains with characteristic hexagonal morphologies[7]. Small additions of Zr ($\leq$ 2 wt.%) have been reported to enhance corrosion resistance, whereas excessive additions promote the formation of insoluble particles within the matrix, which in turn deteriorate corrosion performance[23,24].

The corrosion behavior of biodegradable magnesium alloys is influenced by several factors, including microstructural features (grain size, grain boundaries, and phase distribution), surface characteristics, and the surrounding environment[25]. Heat-treatments, particularly solution and aging treatments, are widely applied to tailor the microstructure and enhance corrosion resistance. Solution treatment involves heating the alloy to a prescribed temperature, holding it for a specific duration, and rapidly quenching to dissolve precipitates or segregations that may serve as corrosion initiation sites. Subsequent aging can further improve the alloy's performance by promoting precipitation hardening and optimizing phase distribution.

For Mg–Gd and Mg–Y-based alloys, achieving optimal peak-aging conditions typically require long aging durations (40 h – 120 h) due to the slow diffusion of Gd and other REEs in the Mg matrix[18]. Binary Mg–Gd alloys with Gd contents below 10 wt.% generally exhibit limited precipitation hardening. However, the addition of other REEs, such as Y, enhances the age-hardening behavior and reduces the total REE content needed, making multi-REE Mg alloys a promising strategy to balance lightweight characteristics with high strength[26].

In this study, a Mg–Y–Gd–Zr alloy was fabricated and systematically characterized, with a focus on microstructural evolution, age-hardening behavior, and corrosion performance. The findings offer valuable insights into how heat treatments and alloying elements affect the properties of biodegradable magnesium alloys, providing guidance for enhanced biomedical applications while addressing ongoing challenges related to corrosion resistance and mechanical integrity.

2 Experimental Procedures

2.1. Alloy fabrication and solution heat-treatment

An Mg alloy ingot with the nominal composition Mg–4.8Y–2.8Gd–0.7Zr was produced using high-purity raw materials: Mg (> 99.97%), Y (99.95%), Gd (99.95%), and Zr (99.9%). The nominal alloy composition was defined based on thermodynamic simulations performed using Thermo-Calc® software, incorporating databases for the Mg–Y–Gd[27], Mg–Zr[28], Gd– Zr[29], and Y–Zr[30] systems. These calculations provided a rational and thermodynamically validated basis for alloy design.

The alloy was melted at 850 °C in a stainless-steel crucible using an electric resistance furnace under a controlled argon atmosphere (min. 99.995%) to prevent oxidation and contamination. The molten alloy was stirred continuously for 15 min to ensure chemical homogeneity before being poured into a preheated graphite mold (75 × 55 × 15 mm). The ingot and mold were allowed to cool to room temperature under argon flow, maintaining alloy purity during solidification. The ingot was studied in the as-cast as well as heat-treated conditions to specifically investigate the effects of solution and aging heat-treatments on the original solidification microstructure and corrosion behavior, avoiding influences from prior plastic deformation.

As-cast samples were subjected to solution heat-treatment to homogenize the microstructure and dissolve segregated secondary phases. The treatment consisted of heating at 525 °C for 24 h in a sealed quartz tube under an argon atmosphere to prevent oxidation, followed by rapid water quenching to retain the homogenized structure and suppress undesired precipitation.

2.2. Age-hardening behavior

The solution heat-treated samples were aged at 250 °C for 1 h, 10 h, 30 h, 60 h, 100 h, and 200 h under an argon atmosphere (min. 99.995%) in sealed quartz tubes to prevent oxidation and ensure consistent thermal conditions. After aging, samples were water-quenched to preserve the microstructural modifications induced by the heat treatment. This temperature and time range was selected to capture the classic precipitation-controlled age-hardening response of Mg–REE alloys[31] and to construct the corresponding age-hardening curve.

The age-hardening curve was determined from Vickers microhardness measurements using a Buehler Micromet 2004 tester with a 100 gf load and a 15 s dwell time. For statistical reliability, 30 measurements were taken at randomly selected locations on each sample for every aging condition. This approach was employed to identify the treatment offering the optimal balance between mechanical performance and corrosion resistance. A similar methodology was reported by Freitas et al.[32] for Mg-based alloys developed for biomedical applications. The experimental design also enabled a direct correlation between the hardening behavior and corrosion performance, providing a mechanistic framework to assess how microstructural strengthening influences degradation pathways in Mg alloys.

2.3. Microstructural characterization

The samples were characterized in terms of semi-quantitative and qualitative chemical composition, phase constituents, and corrosion products using a Hitachi Tabletop Scanning Electron Microscope (SEM, TM3000 series) equipped with an Energy Dispersive X-ray Spectrometer (EDX) operating in Backscattered Electron (BSE) mode.

Grain size measurements were performed on etched samples using a Leica DM 4000M Light Optical Microscope (LOM), following the Heyn intercept method (ASTM E112-24(2024))[33]. Image analysis for microstructural and corrosion layer characterizations were conducted according to ASTM E1382-97(2023)[34], which provides statistically reliable results based on systematic intercepting counting.

For microstructural characterization, at least five micrographs were analyzed per condition to ensure reproducibility, while for EDS measurements, at least three areas were analyzed per condition. EDS analyses were performed in conjunction with the SEM system using magnifications of 100x and 2000x. In addition, to assess the chemical homogeneity of the produced ingots, at least three EDS area measurements were performed in the upper, central, and lower regions of the ingot cross-section.

For LOM and SEM analyses, samples were ground with SiC abrasive papers up to 4000 grit, polished with 1 µm diamond suspension, and etched using a solution of 6 g picric acid in 100 ml ethanol, 6 ml acetic acid, and 10 ml distilled water. This etching procedure effectively revealed grain boundaries and phase constituents, enabling reliable microstructural evaluation.

To identify corrosion products, X-ray diffraction (XRD) analysis was performed using a PANalytical Empyrean diffractometer with Mo-Kα radiation, operating at 40 kV and 30 mA. Scans were conducted over a 2θ range of 12°–35° with a step size of 0.02° and a counting time of 150 s per step. Diffraction patterns were analyzed against the Inorganic Crystal Structure Database (ICDD) to identify secondary phases formed during solidification and heat treatment, supporting the interpretation of microstructural evolution and corrosion products.

2.4. Electrochemical tests

Electrochemical measurements were performed using a three-electrode cell configuration, consisting of an Ag|AgCl/($KCl_{sat.}$) reference electrode, a platinum grid counter electrode, and the alloy samples (exposed area: 1.5 cm^2) as the working electrode. Prior to testing, samples were prepared by sequential grinding with SiC papers (320–4000 grit), polishing with 1 µm diamond paste, ultrasonic cleaning in ethanol, and drying in warm air. These preparation steps ensured a smooth and uniform surface, minimizing artifacts that could affect corrosion dynamics.

Electrochemical tests were conducted in a quiescent, aerated 0.9 wt.% NaCl solution prepared from analytical-grade reagents and deionized water (pH 7.4 ± 0.2), maintained at 37 °C ± 0.1 °C, without prior deaeration, in order to better reproduce physiological conditions.

Potentiodynamic polarization curves were recorded after stabilizing the open-circuit potential (E_{oc}) in the electrolyte. The polarization scan began at −0.5 V vs. Ag|AgCl/($KCl_{sat.}$) relative to E_{oc}, at a sweep rate of 1 $mV.s^{-1}$[35,36] and ended when the total current reached 0.1 A to minimize artificial surface damage[37]. Measurements were obtained using a Solartron 1287A potentiostat controlled by CorrWare® software, with subsequent data fitting and analysis performed using CorrView® software (Scribner Associates). Experimental parameters were chosen to minimize artifacts and ensure reliable evaluation of anodic and cathodic behaviors.

Electrochemical Impedance Spectroscopy (EIS) was performed after 30 min of stabilization at open-circuit potential. A sinusoidal AC perturbation of 10 mV (rms) was applied over a frequency range of 10 kHz to 10 mHz, with data acquired at 10 points per decade. Experiments were performed using a Solartron 1287A potentiostat/galvanostat coupled with a 1260 frequency response analyzer (FRA). Data was processed using ZView® and ZPlot® software (Scribner Associates), with equivalent circuit modeling employed to elucidate corrosion mechanisms. All measurements were performed inside a Faraday cage to minimize electromagnetic interference.

The corrosion potential was monitored before and after each test. Any significant deviation indicated instability, requiring adjustments to the experimental setup or additional stabilization time.

After electrochemical testing, corrosion products were removed by immersing samples in a solution of 200 $g{\cdot}L^{-1}$ CrO_3 + 10 $g{\cdot}L^{-1}$ $AgNO_3$ at 23 °C ± 2 °C for 1 min, following ASTM G1-25[38]. Cleaned surfaces were subsequently examined by SEM/EDS to evaluate corrosion morphology and identify residual products.

3. Results and Discussion

Table 1 presents the semi-quantitative chemical composition of the Mg–Y–Gd–Zr alloy, determined by Energy-Dispersive X-ray Spectroscopy (EDS), as well as the intended manufacturing values. Magnesium and gadolinium concentrations closely match the targets, demonstrating consistency in the overall alloy composition. However, the yttrium concentration is slightly lower than the theoretical value, which may influence the formation of secondary phases such as $Mg_5(Gd,Y)$ and $Mg_{24}Y_5$, with potential impacts on alloy properties[13]. In addition, the zirconium content is significantly below the target value. Because Zr plays a key role in grain refinement during solidification, its reduced concentration does not affect the interpretation of the heat-treatment-induced microstructural evolution addressed in this work. Thus, the final alloy composition obtained was Mg–4.1Y–2.8Gd–0.1Zr (wt.%).

3.1. Microstructure in the as-cast and solution heat-treated conditions

Figure 1 illustrates the microstructure of the Mg–Y–Gd–Zr alloy in the as-cast condition. Phase segregation is evident, characterized by light-colored particles homogeneously distributed in the interdendritic regions. These features reflect a non-uniform distribution of alloying elements and the presence of secondary phases. While such phases can act

Table 1. EDS semi-quantitative chemical analysis results of the produced alloy: measured data and nominal values.

Elements	Measured composition (wt.%)	Nominal composition (wt.%)
Mg	93.0 ± 0.2	91.7
Y	4.1 ± 0.1	4.8
Gd	2.8 ± 0.2	2.8
Zr	0.1 ± 0.1	0.7

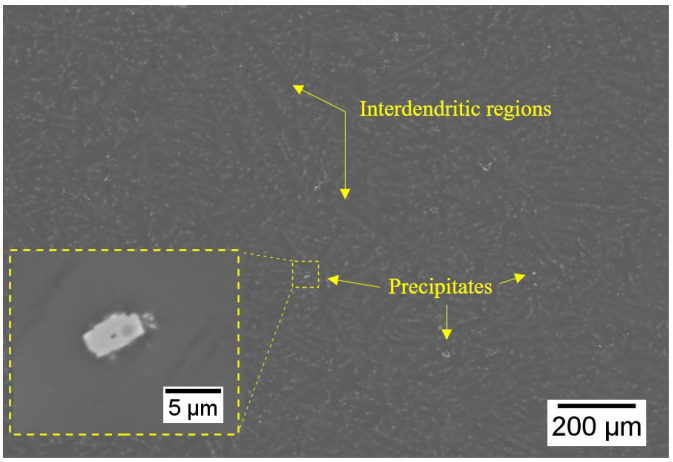

Figure 1. SEM/BSE micrograph of the Mg–4.1Y–2.8Gd–0.1Zr alloy in the as-cast condition.

as barriers to corrosion by limiting anodic dissolution and influencing localized electrochemical behavior [39], the as-cast microstructure generally exhibits suboptimal mechanical properties. This is primarily due to the coarse dendritic grains, uneven phase distribution, and stress concentration sites at interdendritic regions, which can reduce yield strength, ductility, and fatigue resistance[40].

The microstructure of the alloy after solution heat-treatment at 525 °C for 24 h is shown in Figure 2. In Figure 2a, the previously observed dendritic structure is no longer present, confirming the homogenizing effect promoted by the solution heat-treatment.

According to Nodooshan et al.[41] and Gao et al.[42], Mg–REE alloys typically exhibit an α-Mg matrix (HCP) containing secondary phases such as $Mg_5(Gd,Y)$ segregated along grain boundaries, irregular Y-rich compounds (e.g., MgY, $Mg_{24}Y_5$), and Zr-rich precipitates distributed within the matrix and around the secondary phases. However, in the present work these phases could not be clearly, which is consistent with their dissolution into the α-Mg matrix during homogenization. Under these conditions, REEs are redistributed in solid solution, and their associated phases may fall below the spatial and compositional resolution limits of SEM/EDS and XRD. This behavior does not indicate loss of REEs, but rather reflects their effective solubilization, as expected for properly conducted solution heat-treatments.

These phases are reported to influence corrosion behavior because Y, Gd, and Zr, whether as intermetallics or in elemental form, are less electrochemically active than Mg, acting as cathodes and promoting localized galvanic corrosion[43-45]. Liu et al.[46] showed that in 0.1 mol·L^{-1} NaCl solution, higher Y content increase corrosion due to the presence of Y containing intermetallics; however, in 0.1 mol·L^{-1} Na_2SO_4 solution, Y contents above 3 wt.% reduced corrosion, attributed to the formation of a more protective surface film despite the presence of intermetallic phases.

Given Gd's high solubility in Mg, solid-solution strengthening may be favored, whereas Y and Zr can contribute to grain refinement and localized passivation, thus reducing the active surface area and mitigating galvanic effects.

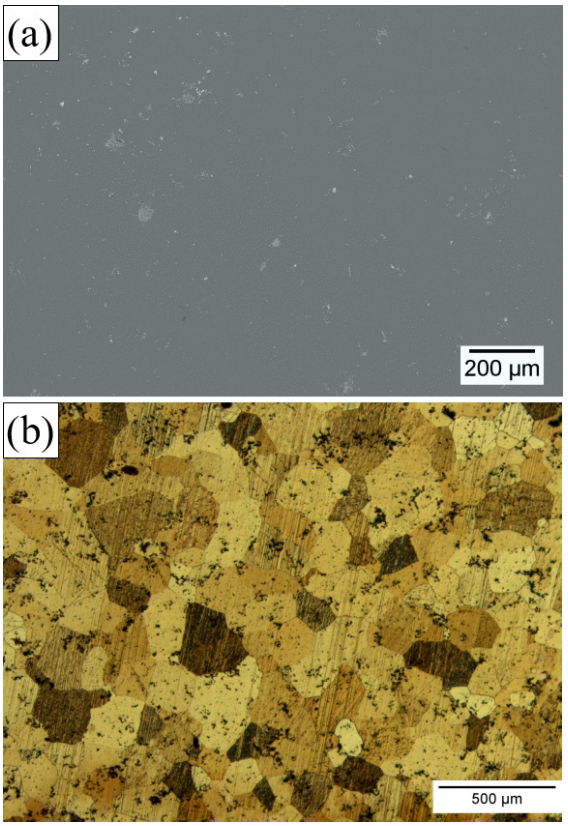

Figure 2. (a) SEM/BSE and (b) LOM micrographs of the Mg–4.1Y–2.8Gd–0.1Zr alloy after solution heat-treatment at 525 °C for 24 h.

Figure 2b (LOM) reveals an equiaxed grain structure with an average grain size of 135.7 µm ± 4.1 µm. Microstructural parameters such as grain size and phase distribution are critical factors governing the corrosion behavior of Mg alloys[45-47]. In this work, the focus was on overall corrosion behavior; therefore, a detailed characterization of precipitates and their local electrochemical effects was considered beyond the scope of this study.

Additional supporting data related to phase identification and thermodynamic prediction are provided in the Supplementary Material.

3.2. Age-hardening behavior

Aging treatments were applied exclusively to samples that had been previously solution heat-treated at 525 °C for 24 h. Figure 3 shows the aging curve of the Mg–Y–Gd–Zr alloy at 250 °C for various times. After 100 h, the alloy reached a peak hardness of 80 HV ± 5 HV, corresponding to an increase of approximately 25% compared to the solution heat-treated sample at 525 °C for 24 h, which had a hardness of 64 HV ± 4 HV, while the as-cast condition got a hardness of 67 HV ± 4 HV. The specimen aged for 200 h showed a hardness value close to that of the 100 h condition (77 HV ± 6 HV). The scatter observed in the hardness values can be attributed to local variations associated with the interaction between the indenter and the dispersed precipitates, whose spatial distribution is not uniformly sampled during each indentation.

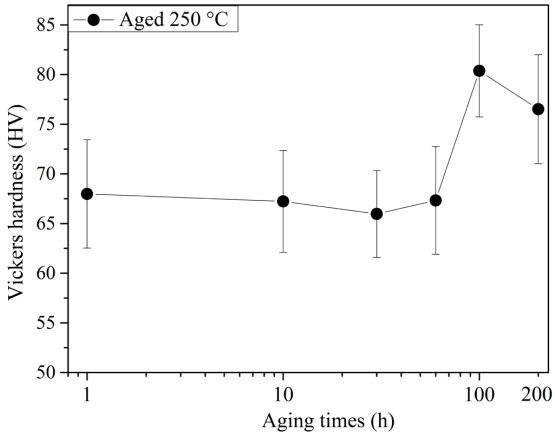

Figure 3. Hardness evolution of the Mg–4.1Y–2.8Gd–0.1Zr alloy during aging at 250 °C

Age hardening is likely governed by the combined effects of precipitate size, precipitate volume fraction and grain size. Qualitative observations from Figures 4a–b show that the 200 h aged sample contains a greater number of large precipitates compared to the 100-h aged sample. Grain size is also influenced by aging: the 100-h aged sample has an average grain size of 86.4 µm ± 2.5 µm, whereas the 200-h aged sample exhibits a significantly larger average grain size of 124.6 µm ± 28.7 µm, with abnormal grain growth contributing to the increased variability in grain size (Figures 4c–d). Despite the smaller grain size at 100 h, these findings are consistent with Xu et al.[48], who reported that, for Mg–Gd–Zr alloys with similar Gd contents, hardness was nearly insensitive to grain size, while hardness increased linearly with Gd content due to precipitation of second phases. Likewise, Anyanwu et al.[49] found that fine precipitates primarily drive age hardening in Mg–Y–Gd–Zr alloys as Gd content increases, whereas higher Y contents are associated with improved elongation. Overall, fine precipitates play the primary role in hardness improvement during aging, while grain size exerts a secondary influence.

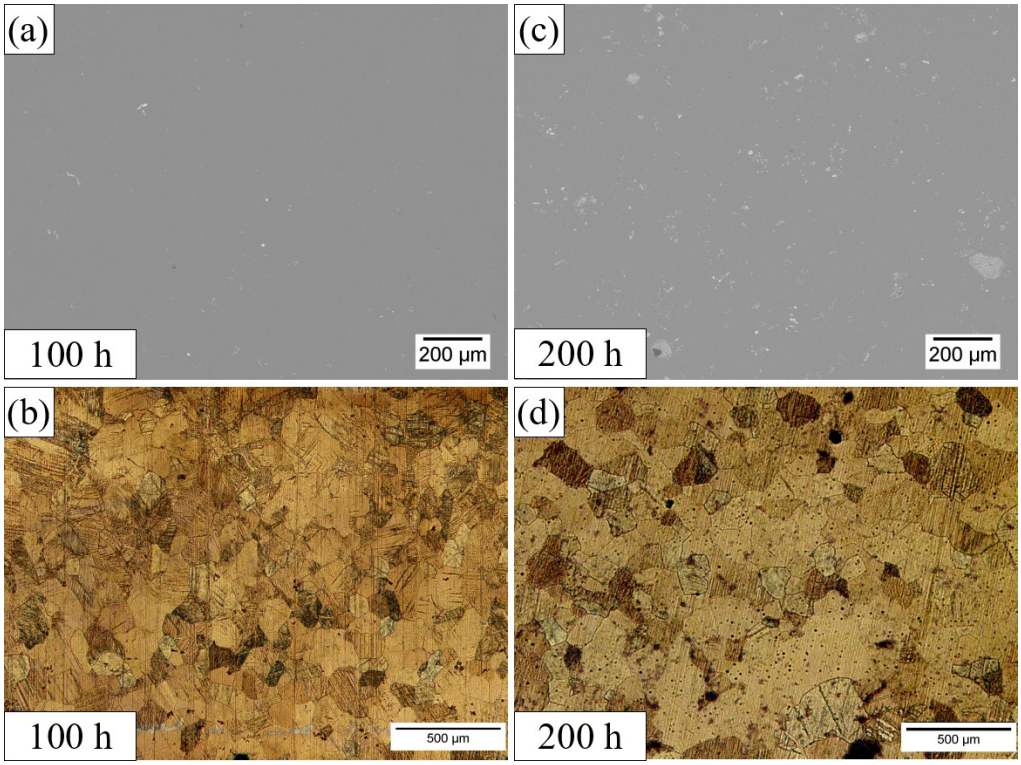

Figure 4. SEM/BSE and LOM micrographs of the Mg–4.1Y–2.8Gd–0.1Zr alloy after solution heat-treatment at 525 °C for 24 h and subsequent aging at 250 °C for (a,b) 100 h and (c,d) 200 h.

3.3. Electrochemical behavior of the alloy in the as-cast, solution heat-treated and aged conditions

Open-circuit potential (E_{oc}) measurements provide insight into the initial surface reactivity and the early evolution of corrosion products at the alloy/electrolyte interface[50]. The initial and stabilized E_{oc} values obtained in an aerated 0.9 wt.% NaCl solution at 37 °C ± 0.1 °C (pH 7.4 ± 0.2), are presented in Table 2. For all conditions, E_{oc} shifted toward more positive values during the first minutes of immersion, indicating progressive formation of a non-conductive corrosion-product layer that modifies the electrical double layer[51]. In chloride-containing media, this layer remains only partially protective due to continuous destabilization by Cl^- ions[45,52].

At the moment of immersion (t = 0 min), the as-cast and solution heat-treated samples exhibited slightly more negative potentials (−1.72 V and −1.69 V vs. Ag|AgCl/($KCl_{sat.}$), respectively), indicating higher initial surface reactivity associated with microstructural heterogeneity and exposure of secondary phases (Figures 1 and 2). After 30 min, E_{oc} values for all conditions converged to a narrow range (−1.59 V to −1.54 V vs Ag|AgCl/($KCl_{sat.}$)), suggesting that different microstructural states evolve toward comparable thermodynamic surface conditions under the present exposure time.

Figure 5 shows anodic and cathodic potentiodynamic polarization curves after potential stabilization for the as-cast alloy, the solution heat-treated at 525 °C for 24 h, and the aged samples. In all conditions, the anodic branches exhibit sustained activity, characterized by a near-linear potential increase followed by a rise at approximately −1.3 V/Ag|AgCl/($KCl_{sat.}$), indicating the absence of stable passivation and continued Mg dissolution in neutral chloride solution. In the cathodic branch, intense gas evolution introduces signal fluctuations that limit the reliability of Tafel extrapolation, as well-known limitation for Mg under these conditions[52-56].

The electrochemical parameters: corrosion potential (E_{corr}), corrosion current density (j_{corr}), and polarization resistance (R_{pp}) obtained by Tafel extrapolation method, are summarized in Table 2. Due to signal fluctuations associated with hydrogen evolution, these values are treated as semi-quantitative and are discussed primarily in terms of comparative trends, as commonly reported for Mg alloys tested under similar testing conditions[6,54]. R_{pp} was calculated using the Stern–Geary relationship ($R_{pp} = B/j_{corr}$), where *B* depends on the anodic and cathodic Tafel slopes [54-56].

A direct comparison between the as-cast and solution heat-treated conditions shows that, although their j_{corr} values remain within the same order of magnitude, the as-cast alloy presents a substantially higher R_{pp} (798 Ω·cm²) than the solution heat-treated sample (413 Ω·cm²). This result indicates that similar j_{corr} values do not necessarily imply identical interfacial conditions, since R_{pp} depends not only on j_{corr} but also on the polarization slopes, which are influenced by surface-layer characteristics and microstructural effects on anodic/cathodic kinetics. In the aerated medium, the observation of H_2 bubbles confirms the occurrence of water reduction; at the same time, oxygen reduction may proceed concurrently, as expected in neutral chloride solutions[45,52-54].

Among the aged conditions, the 100 h sample exhibits the lowest j_{corr} (0.45 mA·cm^{-2}) and the highest R_{pp} (88.9 Ω·cm²). Considering the semi-quantitative nature of the polarization data, this result is discussed as a comparative indication within the aged series. Corrosion behavior is governed by the microstructural state achieved during precipitation rather than by aging time alone. Short aging times (1–10 h)

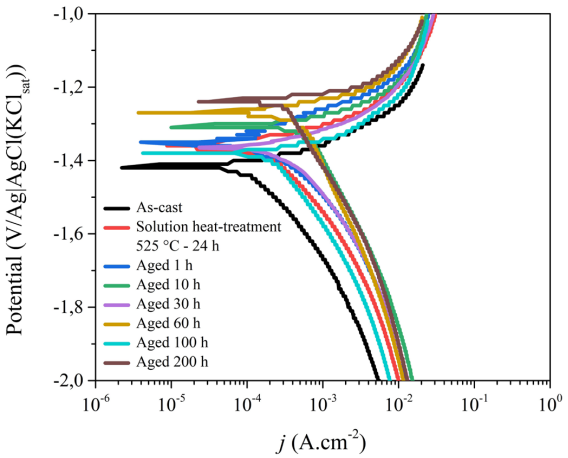

Figure 5. Potentiodynamic polarization curves obtained of the Mg–4.1Y–2.8Gd–0.1Zr alloy in the as-cast, solution heat-treated (525 °C/24 h), and aged conditions in an aerated 0.9 wt.% NaCl solution at 37 °C ± 0.1°C.

Table 2. Electrochemical parameters (Eoc, Ecorr, jcorr) and polarization resistance (Rpp, determined by the Stern–Geary equation) for the as-cast, solution heat-treated, and aged conditions Mg–Y–Gd–Zr alloy samples obtained in an aerated 0.9 wt.% NaCl solution at 37 °C ± 0.1 °C.

Samples	E_{oc} t = 0 min (V/Ag|AgCl$_{(KCl_{sat.})}$)	E_{oc} t = 30 min (V/Ag|AgCl/($KCl_{sat.}$))	Ecorr (V/Ag|AgCl$_{(KCl_{sat.})}$)	jcorr (mA·cm^{-2})	Rpp (Ω·cm²)
As-cast	-1.72	-1.59	-1.43	0.04	798
525 °C-24 h	-1.69	-1.58	-1.35	0.05	413
Aged 1 h	-1.60	-1.58	-1.35	1.03	38.8
Aged 10 h	-1.55	-1.54	-1.31	0.73	54.8
Aged 30 h	-1.59	-1.58	-1.37	1.95	20.5
Aged 60 h	-1.54	-1.55	-1.27	0.96	41.7
Aged 100 h	-1.61	-1.56	-1.38	0.45	88.9
Aged 200 h	-1.57	-1.55	-1.24	0.95	42.1

are consistent with an early stage of precipitation, whereas excessive aging (200 h) is commonly related to precipitate coarsening and increased interfacial heterogeneity. In n contrast, the 100 h condition corresponds to a precipitate size and spatial distribution that, according to established literature for Mg-REE alloys, more effectively mitigates galvanic coupling and favors the development of a more resistive surface layer among the aged states[51,52,56-58].

Electrochemical impedance spectroscopy (EIS) was carried out under the same exposure conditions after E_{oc} stabilization (30 min). Figure 6 presents Nyquist (Figure 6a) and Bode plots (Figures 6b–c) for all conditions.

The impedance spectra exhibit the typical characteristics of magnesium alloys in chloride media, consisting of by two capacitive processes followed by a low-frequency inductive loop[37,39,45,59-61].

In the Nyquist plot (Fig. 6a), two capacitive arcs are observed before the onset of the inductive loop. In contrast, the phase-angle diagram (Fig. 6c) shows a single broad maximum. As discussed by Mansfeld[60], when time constants occur in close frequency ranges and exhibit non-ideal capacitive characteristics, their phase angles may merge into a single broadened maximum, particularly in the presence of low-frequency inductive loop. Similar observations for Mg alloys have been reported by Liu et al.[39] and Orazem and Tribollet[59]. Accordingly, the identification of two capacitive processes is supported primarily by the Nyquist diagram and the change of the |Z| curve in the Bode magnitude plot (Figure 6b).

The as-cast alloy exhibits the largest Nyquist arc and higher impedance values in the medium-frequency range, indicating a more resistive interfacial condition than the solution heat-treated state. Within the aged series, the 100 h sample presents the highest impedance modulus, whereas the 10 h condition shown the lowest |Z| values, confirming that the impedance behavior is strongly governed by the microstructural state, which controls the formation and stability of the corrosion-product layer.

Equivalent-circuit analysis was performed using ZView®, following the approaches reported by Srinivasan et al.[37], and Liu et al.[39], Ascencio et al.[45], Guadarrama-Munõz et al.[61] (Figure 7). The chi-squared (χ^2) values were $\leq 3.9\times10^{-3}$, confirming the quality of the fits and fall within the typical range reported for Mg alloys (10^{-3}–10^{-5}).

In the adopted equivalent circuit, R_e represents the electrolyte resistance. R_1–CPE_1 pair is associated with the high-frequency capacitive process attributed to the corrosion-product layer, whereas R_2–CPE_2 corresponds to the medium-frequency capacitive process related to charge transfer at the film/substrate interface. The inductive elements (L and RL) describe the low-frequency inductive loop commonly reported for Mg corrosion in chloride media[36,45,59,61-64]. Because the inductive loop is weak in most conditions, the quantitative discussion focuses on the resistive and capacitive parameters.

The fitting results (Table 3) show that the as-cast alloy exhibits higher polarization resistance ($R_p = R_1+R_2 = 53.96\ \Omega\cdot cm^2$) than the solution heat-treated sample ($27.20\ \Omega\cdot cm^2$), corroborating with both the impedance spectra and the polarization data (Table 2). Whitin the aged series, R_p increases relative to the solution heat-treated condition, with the 100 h sample the highest value ($42.74\ \Omega\cdot cm^2$), although still lower than the as-cast state ($53.96\ \Omega\cdot cm^2$). These results indicate that aging improves the interfacial condition compared with the solution heat-treated state but does not exceed the resistance associated with the thicker corrosion layer formed on the heterogeneous as-cast surface under the present exposure time.

Overall, the electrochemical results indicate that corrosion behavior is governed by the stability and resistive character of the corrosion-product layer, which are strongly controlled by the microstructural state induced by heat treatment.

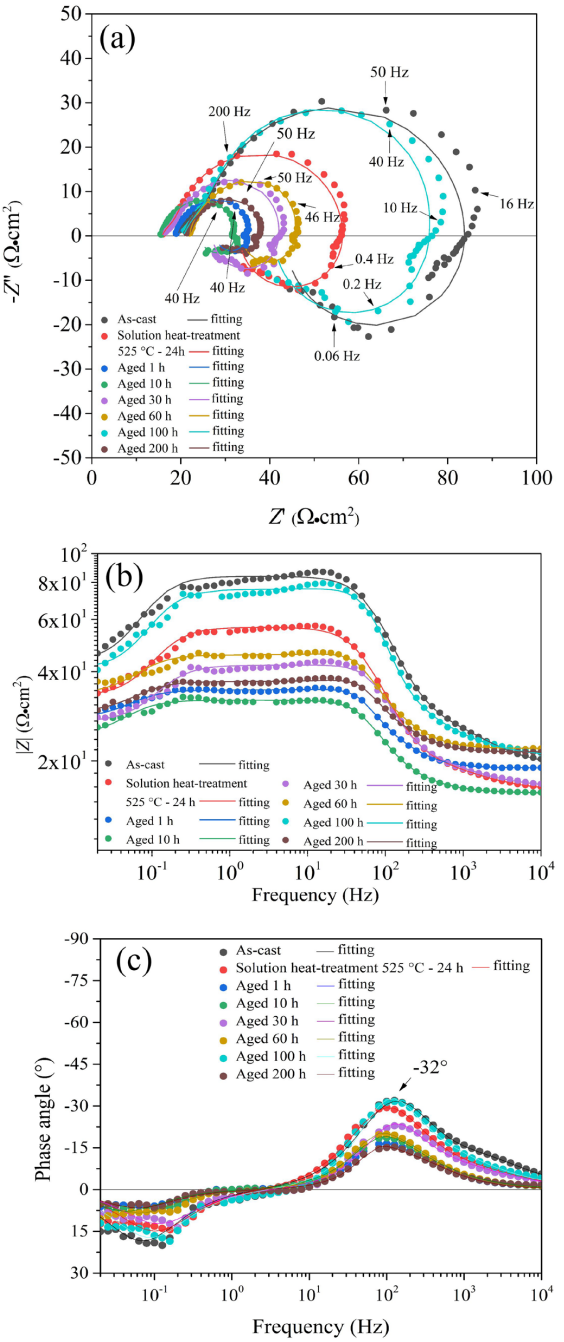

Figure 6. Electrochemical impedance spectra of the Mg–4.1Y–2.8Gd–0.1Zr alloy in the as-cast, solution heat-treated (525 °C/24 h), and aged conditions in an aerated 0.9 wt.% NaCl solution at 37 °C ± 0.1°C: (a) Nyquist, (b) Bode, and (c) phase-angle plots.

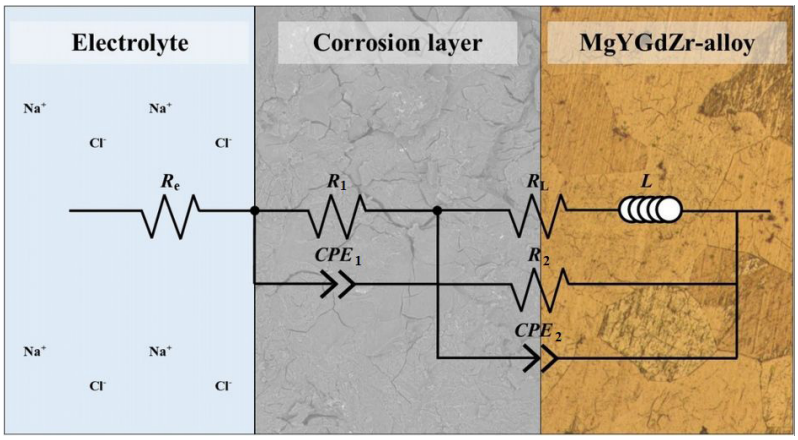

Figure 7. Equivalent electric circuit used to fit the experimental EIS data of the Mg–4.1Y–2.8Gd–0.1Zr alloy immersed in an aerated 0.9 wt.% NaCl solution at 37 °C ± 0.1 °C.

Table 3. Fitting parameters obtained from EIS data for the as-cast, solution heat-treated (525 °C/24 h), and aged Mg–Y–Gd–Zr alloy conditions, using the equivalent circuit shown in Figure 7 ($\chi^2 \leq 3.9\times10^{-3}$).

Samples	R_e (Ω·cm^2)	R_1 (Ω·cm^2)	R_2 (Ω·cm^2)	R_p (R_1+R_2) (Ω·cm^2)	CPE_1 (Ω-1·sn·cm-2)	n_1	CPE_2 (Ω-1·sn·cm-2)	n_2
As-cast	18.69	11.70	42.26	53.96	59.7×10^{-5}	0.72	3.8×10^{-5}	0.80
525 °C–24 h	21.02	8.67	18.53	27.20	78.3×10^{-5}	0.61	7.3×10^{-5}	0.68
Aged 1 h	19.62	8.21	7.09	15.30	1.7×10^{-4}	0.66	7.3×10^{-5}	0.67
Aged 10 h	15.35	6.94	6.69	13.63	2.5×10^{-4}	0.82	10.7×10^{-5}	0.70
Aged 30 h	15.86	9.90	9.53	19.43	1.6×10^{-4}	0.62	7.0×10^{-5}	0.66
Aged 60 h	21.32	7.93	9.04	16.97	1.1×10^{-4}	0.74	4.7×10^{-5}	0.73
Aged 100 h	20.81	14.5	28.24	42.74	2.8×10^{-4}	0.89	5.2×10^{-5}	0.83
Aged 200 h	20.04	3.73	8.53	12.26	1.8×10^{-4}	0.68	4.5×10^{-5}	0.66

3.4. Corrosion products and substrate morphology after potentiodynamic polarization measurements

Corrosion products and substrate morphology were examined after the potentiodynamic polarization measurements conducted in aerated 0.9 wt.% NaCl solution at 37 °C ± 0.1 °C. This analysis aimed to correlate the electrochemical behavior with corrosion-layer formation and with substrate degradation features revealed after chemical removal of the corrosion product.

Both as-cast and solution heat-treated samples exhibited fully corroded surfaces characterized by cracked regions interspersed with more compact areas and dispersed white precipitates, as exemplified for the 525 °C/24 h sample in Figures 8a–b. The cracking is attributed to hydrogen evolution during corrosion, which induces internal stresses within the corrosion layer. This morphology agrees with reports describing a thin MgO film covered by a thicker, porous $Mg(OH)_2$ layer on corroded magnesium surfaces[65]. The dispersed white precipitates act as cathodic phases, promoting localized dissolution of the α-Mg matrix[39].

EDS analysis (Figure 8c) shows that the corrosion layer is predominantly composed of Mg and O, with minor contributions of Cl and rare-earth elements. The low peak intensities of Y and Zr, despite their nominal alloy contents, are attributed to the predominance of $Mg(OH)_2$/MgO in the outer corrosion layer and to the preferential retention of REE-rich phases near the alloy/corrosion-layer interface rather than within the external corrosion products. This interpretation is corroborated by the XRD pattern (Figure 8d), which identifies α-Mg, $MgCl_2$, and $Mg(OH)_2$ as the main corrosion products, with no clear evidence of REE oxides in the outer layer.

After removal of corrosion products, the substrate exhibited large pits (Figure 8e). At higher magnification (Figure 8f), ditches within the α-Mg phase filled with aligned hydrogen pores are observed[66], evidencing localized dissolution associated with hydrogen evolution.

Aged samples exhibited a distinct corrosion morphology. As shown for the 100 h condition (Figure 9a–b), the corrosion layer consists of compact regions combined with a fine, uniform porous structure presenting “petal-like” features, similar to morphologies reported for Mg–Y–Zn–Zr alloys[67].

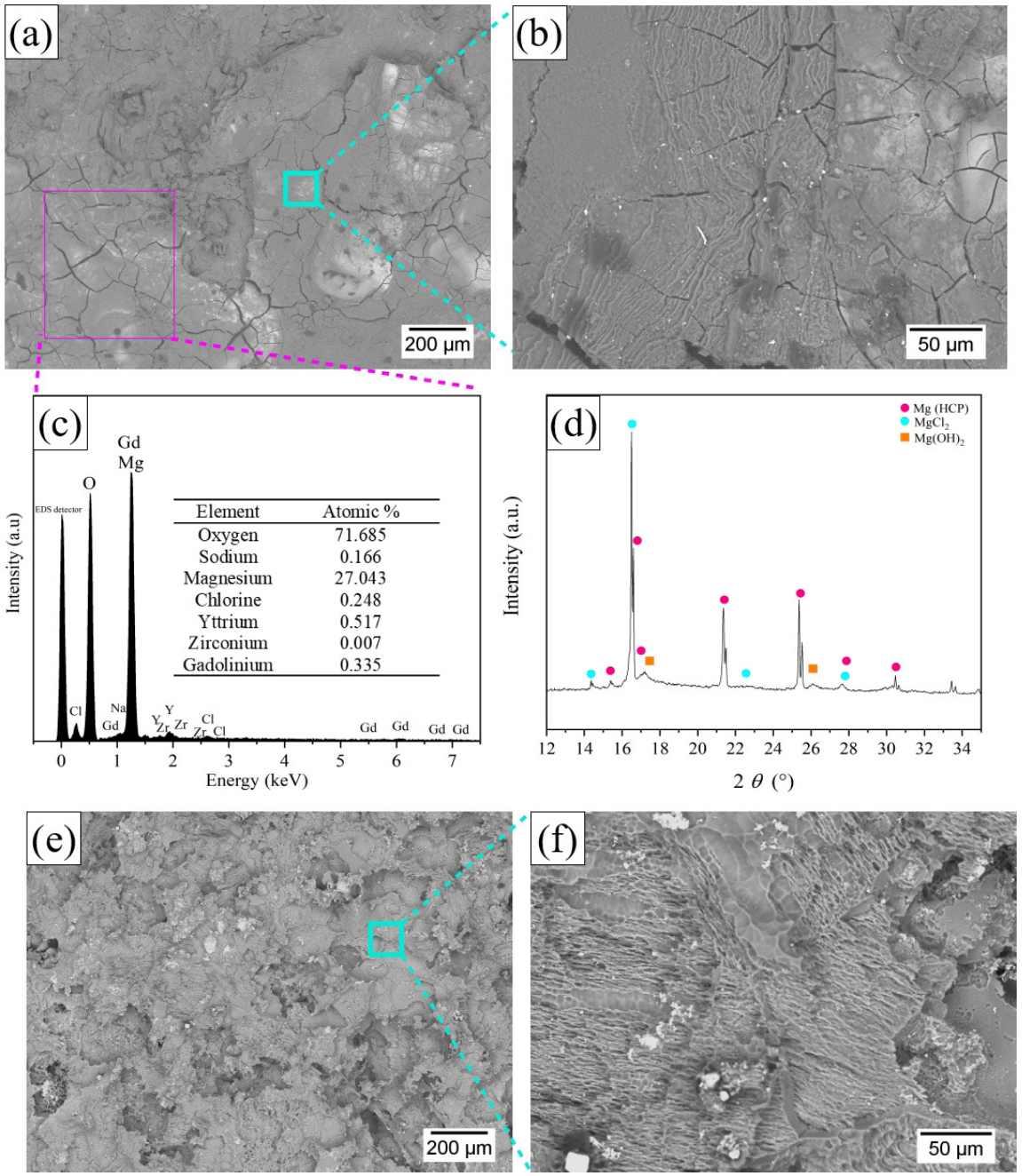

Figure 8. Surface and corrosion-product characterization of the solution heat-treated Mg–4.1Y–2.8Gd–0.1Zr alloy (525 °C/24 h) after potentiodynamic polarization measurements in an aerated 0.9 wt.% NaCl solution at 37 °C ± 0.1 °C. (a) SEM/BSE image of the corroded surface before removal of corrosion products; (b) higher-magnification view of the region highlighted in (a); (c) EDS spectrum acquired from the corrosion layer; (d) XRD pattern of the corrosion products; (e) SEM/BSE image of the substrate after complete removal of corrosion products; (f) higher-magnification SEM/BSE image of the cleaned substrate showing localized attack features.

This morphology differs markedly from the cracked pattern observed for the as-cast and solution heat-treated conditions.

EDS results (Figure 9c) show relatively higher contents of Cl, Y, and Gd within the corrosion layer compared with the non-aged conditions. The XRD pattern (Figure 9f) shows peaks corresponding to α-Mg (HCP), $MgCl_2$, $Mg(OH)_2$, MgO, and $YZrO_{3\cdot5}$. However, the precise stoichiometry of the $YZrO_{3\cdot5}$ phase requires further investigation, its presence indicates participation of REE-rich phases in the corrosion process for the aged conditions.

After removal of corrosion products, the substrate exhibited localized corrosion with large pits (Figure 9d). At higher magnification (Figure 9e), ditches associated with hydrogen evolution are observed, similar to those in the as-cast and solution heat-treated samples[66].

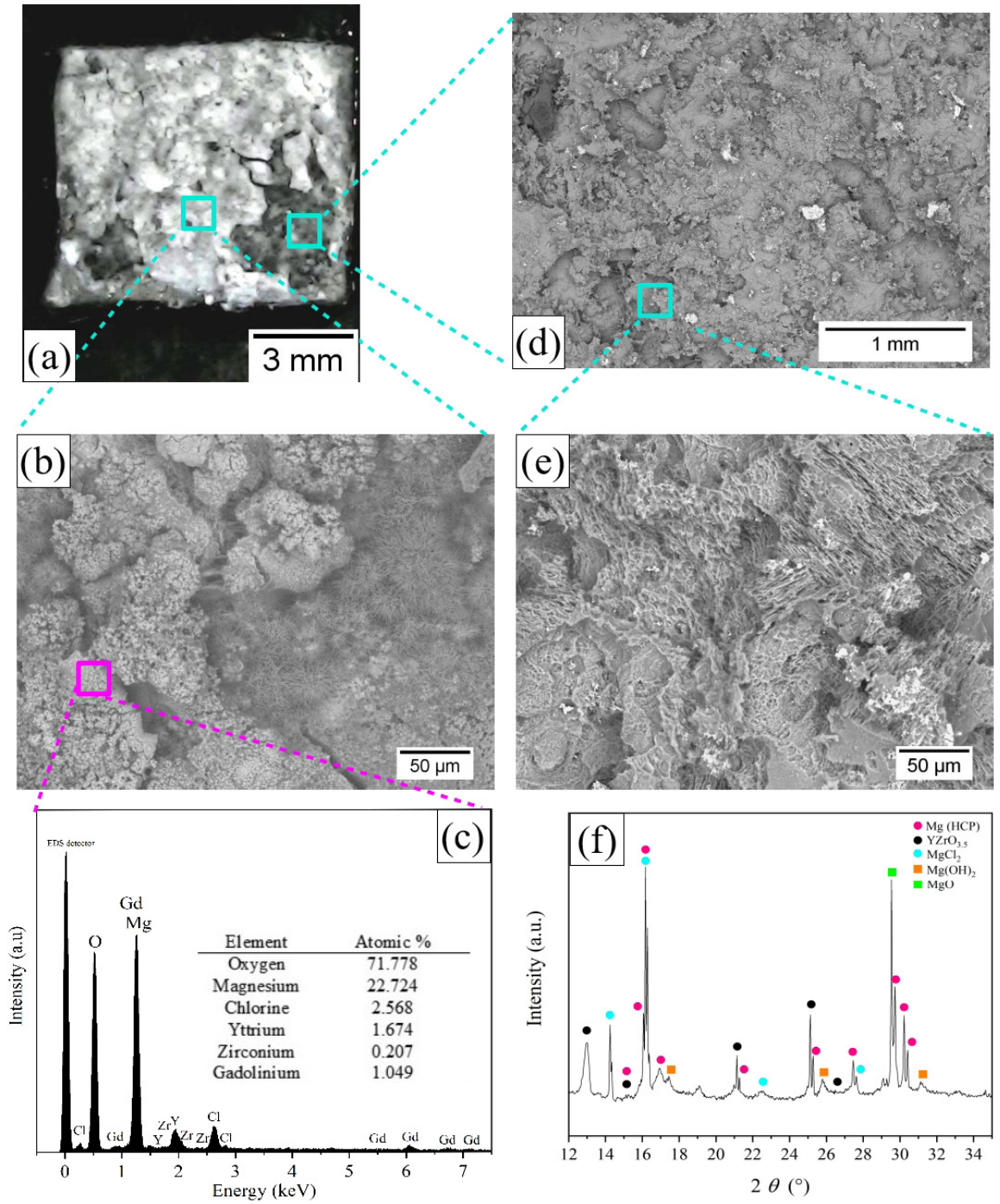

Figure 9. Surface characterization of the Mg–4.1Y–2.8Gd–0.1Zr alloy aged 100 h at 250 °C after potentiodynamic polarization measurements in an aerated 0.9 wt.% NaCl solution at 37 °C ± 0.1 °C: (a,b) SEM/BSE micrographs of corrosion products before cleaning; (c) EDS spectrum; (d,e) SEM/BSE micrographs of the substrate after cleaning; and (f) XRD pattern of the corrosion layer.

4. Conclusions

The corrosion behavior of the Mg–4.1Y– 2.8Gd–0.1Zr alloy (wt.%) in aerated 0.9 wt.% NaCl solution at 37 °C ± 0.1 °C were evaluated for the as-cast, solution heat-treated, and aged conditions using potentiodynamic polarization curves, impedance measurements, and surface characterization.

The as-cast condition exhibited the highest polarization resistance and impedance modulus, associated with formation of a thicker corrosion layer, although its heterogeneous surface favored localized attack. Solution heat-treatment (525 °C/24 h) shifted to potentials to more noble values but produced a thinner and less resistive corrosion layer, resulting in lower R_p and R_{pp} values. Among the aged conditions,

aging at 250 °C for 100 h provided the highest R_p and the most uniform interfacial condition, whereas shorter aging times and overaging (200 h) resulted in more heterogeneous surface films and lower resistance to charge transfer.

These findings emphasize the importance of microstructural control in optimizing the corrosion characteristics of Mg–Y–Gd–Zr alloys for biodegradable applications.

5. Acknowledgements

The authors acknowledge the financial support from the Coordenação de Aperfeiçoamento de Pessoal de Nível Superior (CAPES, Brazil – Finance Code 001), the Conselho Nacional de Desenvolvimento Científico e Tecnológico (CNPq, Brazil – Grant nº. 142337/2019-6), the Fundação de Amparo à Pesquisa de Minas Gerais (FAPEMIG – Grant APQ-00682-24), and the Fundação de Amparo à Pesquisa do Estado de São Paulo (FAPESP, Grants nº. 2018/20375-2 and 2021/02381-8).

6. Data Availability

The data supporting the findings of this study are available within the article and its Supplementary Material.

7. References

1. Chen J, Tan L, Yu X, Etim IP, Ibrahim M, Yang K. Mechanical properties of magnesium alloys for medical application: a review. J Mech Behav Biomed Mater. 2018;87:68-79. https://doi.org/10.1016/j.jmbbm.2018.07.022.
2. Agarwal S, Curtin J, Duffy B, Jaiswal S. Biodegradable magnesium alloys for orthopedic applications: a review on corrosion. Biocompatibility and Surface Modifications Mater Sci Eng C. 2016;68:948-63. https://doi.org/10.1016/j.msec.2016.06.020.
3. Zhang Y, Xu J, Ruan YC, Yu MK, O'Laughlin M, Wise H, et al. Implant-derived magnesium induces local neuronal production of CGRP to improve bone-fracture healing in rats. Nat Med. 2016;22(10):1160-9. https://doi.org/10.1038/nm.4162.
4. Choudhary L, Singh Raman RK, Hofstetter J, Uggowitzer PJ. In-vitro characterization of stress corrosion cracking of aluminium-free magnesium alloys for temporary bioimplant applications. Mater Sci Eng C. 2014;42:629-36. https://doi.org/10.1016/j.msec.2014.06.018.
5. Staiger MP, Pietak AM, Huadmai J, Dias G. Magnesium and its alloys as orthopedic biomaterials: a review. Biomaterials. 2006;27(9):1728-34. https://doi.org/10.1016/j.biomaterials.2005.10.003.
6. Song G. Control of biodegradation of biocompatible magnesium alloys. Corros Sci. 2007;49(4):1696-701. https://doi.org/10.1016/j.corsci.2007.01.001.
7. Ding Y, Wen C, Hodgson P, Li Y. Effects of alloying elements on the corrosion behavior and biocompatibility of biodegradable magnesium alloys: a review. J Mater Chem B. 2014;2(14):1912-33. https://doi.org/10.1039/C3TB21746A.
8. Yang M, Chen C, Wang D, Shao Y, Zhou W, Shuai C, et al. Biomedical rare-earth magnesium alloy: current status and future prospects. J Magnes Alloy. 2024;12(4):1260-82. https://doi.org/10.1016/j.jma.2024.03.014.
9. Calado LM, Carmezim MJ, Montemor MF. Rare earth-based magnesium alloys - a review on WE series. Front Mater. 2022;8:804906. https://doi.org/10.3389/fmats.2021.804906.
10. Jayasathyakawin S, Ravichandran M, Naveenkumar R, Radhika N, Ismail SO, Mohanavel V. Recent advances in magnesium alloys for biomedical applications: a review. Mater Today Commun. 2025;42:111239. https://doi.org/10.1016/j.mtcomm.2024.111239.
11. Chen J, Tan L, Yu X, Yang K. Effect of minor content of Gd on the mechanical and degradable properties of as-cast Mg–2Zn–xGd–0.5Zr alloys. J Mater Sci Technol. 2019;35(4):503-11. https://doi.org/10.1016/j.jmst.2018.10.022.
12. Liu X, Shan D, Song YT, Han E. Influence of yttrium element on the corrosion behaviors of Mg–Y binary magnesium alloy. J Magnes Alloy. 2017;5(1):26-34. https://doi.org/10.1016/j.jma.2016.12.002.
13. Zhang X, Zhang K, Deng X, Hongwei L, Yongjun L, Minglong M, et al. Corrosion behavior of Mg–Y alloy in NaCl aqueous solution. Prog Nat Sci. 2022;22(2):169-74. https://doi.org/10.1016/j.pnsc.2012.03.014.
14. Liang J, Wu S, Li B, Lei B, Chen Y, Jiang M, et al. Microstructure and corrosion behavior of Y-modified ZK60 Mg alloy prepared by laser powder bed fusion. Corros Sci. 2023;211:110895. https://doi.org/10.1016/j.corsci.2022.110895.
15. Seitz J-M, Lucas A, Kirschner M. Magnesium-based compression screws: a novelty in the clinical use of implants. J Miner Met Mater Soc. 2016;68(4):1177-82. https://doi.org/10.1007/s11837-015-1773-1.
16. Guo L, Yu L, Zhao Q, Gong X, Xie H, Yuan G, et al. Biodegradable JDBM coating stent has potential to be used in the treatment of benign biliary strictures. Biomed Mater. 2021;16(2):025010. https://doi.org/10.1088/1748-605X/abda88.
17. Xu L-H, Ye L-T, Wang J-Y, Qiu X. Magnesium-based alloys for bone regeneration and beyond: A review of advances and therapeutic prospects. Regen Ther. 2025;30:977-83. https://doi.org/10.1016/j.reth.2025.10.010.
18. Xie K, Wang L, Guo Y, Zhao S, Yang Y, Dong D, et al. Effectiveness and safety of biodegradable Mg-Nd-Zn-Zr alloy screws for the treatment of medial malleolar fractures. J Orthop Translat. 2021;27:96-100. https://doi.org/10.1016/j.jot.2020.11.007.
19. Feyerabend F, Fischer J, Holtz J, Witte F, Willumeit R, Drücker H, et al. Evaluation of short-term effects of rare earth and other elements used in magnesium alloys on primary cells and cell lines. Acta Biomater. 2010;6(5):1834-42. https://doi.org/10.1016/j.actbio.2009.09.024.
20. Zheng YF, Gu XN, Witte F. Biodegradable metals. Mater Sci Eng Rep. 2014;77:1-34. https://doi.org/10.1016/j.mser.2014.01.001.
21. Kirkland NT, Birbilis N, Staiger MP. Assessing the corrosion of biodegradable magnesium implants: A critical review. Acta Biomater. 2012;8(3):925-36. https://doi.org/10.1016/j.actbio.2011.11.014.
22. Li H, Wang P, Lin G, Huang J. The role of rare earth elements in biodegradable metals: A review. Acta Biomater. 2021;129:33-42. https://doi.org/10.1016/j.actbio.2021.05.014.
23. Fu W, Wang RH, Xue H, Kuang J, Zhang JY, Liu G, et al. Effects of Zr addition on the multi-scale second-phase particles and fracture behavior for Mg-3Gd-1Zn alloy. J Alloys Compd. 2018;747:197-210. https://doi.org/10.1016/j.jallcom.2018.02.328.
24. Qian M, Das A. Grain refinement of magnesium alloys by zirconium: formation of equiaxed grains. Scr Mater. 2006;54(5):881-6. https://doi.org/10.1016/j.scriptamat.2005.11.002.
25. Song Y, Shan D, Han EH. Pitting corrosion of a rare earth Mg alloy GW93. J Mater Sci Technol. 2017;33(9):954-60. https://doi.org/10.1016/j.jmst.2017.01.014.
26. Li G, Zhang J, Wu R, Liu S, Song B, Jiao Y, et al. Improving age hardening response and mechanical properties of a new Mg–RE alloy via simple pre-cold rolling. J Alloys Compd. 2019;777:1375-85. https://doi.org/10.1016/j.jallcom.2018.11.082.
27. Guo C, Du Z, Li C. A thermodynamic description of the Gd–Mg–Y system. Calphad. 2007;31(1):75-88. https://doi.org/10.1016/j.calphad.2006.10.004.
28. Arroyave R, Shin D, Liu ZK. Modification of the thermodynamic model for the Mg–Zr system. Calphad. 2005;29(3):230-8. https://doi.org/10.1016/j.calphad.2005.07.004.

29. Bo H, Liu LB, Hu JL, Zhang XD, Jin ZP. Thermodynamic re-assessment of the Al–Gd and Gd-Zr systems. Thermochim Acta. 2014;591:51-6. https://doi.org/10.1016/j.tca.2014.07.014.
30. He XC, Liu HS. Determination of the isothermal section of the Cu–Zr–Y ternary system at 978 K. J Alloys Compd. 2009;475(1-2): 245-51. https://doi.org/10.1016/j.jallcom.2008.07.144.
31. He SM, Zeng XQ, Peng LM, Gao X, Nie JF, Ding WJ. Microstructure and strengthening mechanism of high strength Mg-10Gd-2Y-0.5 Zr alloy. J Alloys Compd. 2007;427(1-2):316-23. https://doi.org/10.1016/j.jallcom.2006.03.015.
32. Freitas BX, Antonini LA, Cury PLCT, Da Silva VLF, Chaia N, Tomachuk CR, et al. Microstructural evolution and electrochemical behavior of solution treated, hot rolled and aged MgDyZnZr alloy. Metals. 2021;11(11):1855. https://doi.org/10.3390/met11111855.
33. ASTM: American Society for Testing and Materials. ASTM E112-24: standard test method for determining average grain size. West Conshohocken: ASTM; 2024. https://doi.org/10.1520/E0112-24.
34. ASTM: American Society for Testing and Materials. ASTM-E1382-97: standard test methods for determining average grain size using semiautomatic and automatic image analysis. West Conshohocken: ASTM; 2023. https://doi.org/10.1520/E1382-97R23.
35. Chang JW, Fu PH, Guo XW, Peng LM, Ding WJ. The effects of heat treatment and zirconium on the corrosion behavior of Mg–3Nd–0.2Zn–0.4Zr (w%) alloy. Corros Sci. 2007;49(6):2612-27. https://doi.org/10.1016/j.corsci.2006.12.011.
36. Anik M, Celikten G. Analysis of the electrochemical reaction behavior of alloy AZ91 by EIS technique in H_3PO_4/KOH buffered K_2SO_4 solutions. Corros Sci. 2007;49(4):1878-94. https://doi.org/10.1016/j.corsci.2006.10.016.
37. Srinivasan A, Blawert C, Huang Y, Mendis CL, Kainer KU, Hort N. Corrosion behavior of Mg–Gd-Zn based alloys in aqueous NaCl solution. J Magnes Alloy. 2014;2(3):245-56. https://doi.org/10.1016/j.jma.2014.08.002.
38. ASTM: American Society for Testing and Materials. ASTM G1-25: standard practice for preparing, cleaning and evaluating corrosion test. West Conshohocken: ASTM; 2025. https://doi.org/10.1520/G0001-25.
39. Liu J, Yang L, Zhang C, Zhang B, Zhang T, Li Y, et al. Significantly improved corrosion resistance of Mg-15Gd-2Zn-0.39Zr alloys: effect of heat-treatment. Mater Sci Technol. 2019;35(8):1644-54. https://doi.org/10.1016/j.jmst.2019.03.027.
40. Trivedi P, Nune KC, Misra RDK, Goel S, Jayganthan R, Srinivasan A. Grains refinement to submicron regime in multiaxial forged Mg-2Zn-Gd alloy and relationship to mechanical properties. Mater Sci Eng A. 2016;668:59-65. https://doi.org/10.1016/j.msea.2016.05.050.
41. Nodooshan HRJ, Liu W, Wu G, Rao Y, Zhou C, He S, et al. Effect of Gd content on microstructure and mechanical properties of Mg–Gd–Y–Zr alloys under peak-aged condition. Mater Sci Eng A. 2014;615:79-86. https://doi.org/10.1016/j.msea.2014.07.056.
42. Gao L, Chen RS, Han EH. Microstructure and strengthening mechanisms of a cast Mg-1.48Gd-1.13Y-0. 16Zr (at.%) alloy. J Mater Sci. 2009;44(16):4443-54. https://doi.org/10.1007/s10853-009-3672-8.
43. Witte F, Hort N, Vogt C, Cohen S, Kainer KU, Willumeit R, et al. Degradable biomaterials based on magnesium corrosion. Curr Opin Solid State Mater Sci. 2008;12(5-6):63-72. https://doi.org/10.1016/j.cossms.2009.04.001.
44. Kutniy KV, Papirov II, Tikhonovsky MA, Pikalov AI, Sivtzov SV, Pirozhenko LA, et al. Influence of grain size on mechanical and corrosion properties of magnesium alloy for medical implants. Materialwiss Werkstofftech. 2009;40(4):242-6. https://doi.org/10.1002/mawe.200900434.
45. Ascencio M, Pekguleryuz M, Omanovic S. An investigation of the corrosion mechanisms of WE43 Mg alloy in a modified simulated body fluid solution: the influence of immersion time. Corros Sci. 2014;87:489-503. https://doi.org/10.1016/j.corsci.2014.07.015.
46. Liu M, Schmutz P, Uggowitzer PJ, Song G, Atrens A. The influence of yttrium (Y) on the corrosion of Mg–Y binary alloys. Corros Sci. 2010;52(11):3687-701. https://doi.org/10.1016/j.corsci.2010.07.019.
47. Argade GR, Panigrahi SK, Mishra RS. Effects of grain size on the corrosion resistance of wrought magnesium alloys containing neodymium. Corros Sci. 2012;58:145-51. https://doi.org/10.1016/j.corsci.2012.01.021.
48. Xu Y, Gensch F, Ren Z, Kainer KU, Hort N. Effects of Gd solutes on hardness and yield strength of Mg alloys. Prog Nat Sci. 2018;28(6):724-30. https://doi.org/10.1016/j.pnsc.2018.10.002.
49. Anyanwu IA, Kamado S, Kojima Y. Aging characteristics and high temperature tensile properties of Mg–Gd–Y–Zr alloys. Mater Trans. 2001;42(7):1206-11. https://doi.org/10.2320/matertrans.42.1206.
50. Jamesh MI, Wu G, Zhao Y, McKenzie DR, Bilek MMM, Chu PK. Electrochemical corrosion behavior of biodegradable Mg–Y–RE and Mg–Zn–Zr alloys in Ringer's solution and simulated body fluid. Corros Sci. 2015;91:160-84. https://doi.org/10.1016/j.corsci.2014.11.015.
51. Chen Z. The open-circuit potential of a polarizable and reactive electrode. ECS Trans. 2008;6(24):1-15. https://doi.org/10.1149/1.2900649.
52. Gomes MP, Costa I, Pébère N, Rossi JL, Tribollet B, Vivier V. On the corrosion mechanism of Mg investigated by electrochemical impedance spectroscopy. Electrochim Acta. 2019;306:61-70. https://doi.org/10.1016/j.electacta.2019.03.080.
53. Song G-L, Atrens A. Understanding magnesium corrosion: A framework for improved alloy performance. Adv Eng Mater. 2003;5(12):837-58. https://doi.org/10.1002/adem.200310405.
54. Bard AJ, Faulkner LR, White HS. Electrochemical methods: fundamentals and applications. 3rd ed. Hoboken: John Wiley&Sons; 2022.
55. Stern M, Geaby AL. Electrochemical polarization: I. A theoretical analysis of the shape of polarization curves. J Electrochem Soc. 1957;104(1):56. https://doi.org/10.1149/1.2428496.
56. Song GL, Atrens A. Corrosion mechanisms of magnesium alloys. Adv Eng Mater. 1999;1(1):11-33. https://doi.org/10.1002/(SICI)1527-2648(199909)1:1<11::AID-ADEM11>3.0.CO;2-N.
57. Jana A, Das M, Balla VK. Effect of heat-treatment on microstructure, mechanical, corrosion and biocompatibility of Mg–Zn–Zr–Gd–Nd alloy. J Alloys Compd. 2020;821:153462. https://doi.org/10.1016/j.jallcom.2019.153462.
58. Chen J, Tan L, Yu X, Yang K. Effect of minor content of Gd on the mechanical and degradable properties of as-cast Mg–2Zn–xGd–0.5Zr alloys. J Mater Sci Technol. 2019;35(4):503-11. https://doi.org/10.1016/j.jmst.2018.10.022.
59. Orazem ME, Tribollet B. Electrochemical impedance spectroscopy. Hoboken: John Wiley&Sons; 2008. https://doi.org/10.1002/9780470381588.
60. Mansfeld F. Use of electrochemical impedance spectroscopy for the study of corrosion protection by polymer coatings. J Appl Electrochem. 1995;25(3):187-202. https://doi.org/10.1007/BF00262955.
61. Guadarrama-Muñoz F, Mendoza-Flores J, Duran-Romero R, Genesca J. Electrochemical study on magnesium anodes in NaCl and $CaSO_4$-$Mg(OH)_2$ aqueous solutions. Electrochim Acta. 2006;51(8-9):1820-30. https://doi.org/10.1016/j.electacta.2005.02.144.
62. Hanna A, Rabahi L, Soualili A, Dakhouche A, Bradai D, Azzeddine H. On the corrosion behaviour of as-cast and heat-treated Mg-REE alloys in 0.9% NaCl solution. J. Met. Mater. Miner. 2020;30(1):29-39. https://doi.org/10.55713/jmmm.v30i1.600.

63. Baril G, Pébère N. The corrosion of pure magnesium in aerated and desaerated sodium sulphate solutions. Corros Sci. 2001;43(3):471-84. https://doi.org/10.1016/S0010-938X(00)00095-0.
64. Baril G, Galicia G, Deslouis C, Pébère N, Tribollet B, Vivier V. An impedance investigation of the mechanism of pure magnesium corrosion in sodium sulfate solutions. J Electrochem Soc. 2007;154(2):C108-13. https://doi.org/10.1149/1.2401056.
65. Galicia G, Pébère N, Tribollet B, Vivier V. Local and global electrochemical impedances applied to the corrosion behaviour of an AZ91 magnesium alloy. Corros Sci. 2009;51(8):1789-94. https://doi.org/10.1016/j.corsci.2009.05.005.
66. Liu X, Xue J, Zhang D. Electrochemical behaviors and discharge performance of the as-extruded Mg-1.5 wt%Ca alloys as anode for Mg-air battery. J Alloys Compd. 2019;790:822-8. https://doi.org/10.1016/j.jallcom.2019.03.260.
67. Bao L, Zhang Z, Le Q, Zhang S, Cui J. Corrosion behavior and mechanism of Mg–Y–Zn–Zr alloys with various Y/Zn mole ratios. J Alloys Compd. 2017;712:15-23. https://doi.org/10.1016/j.jallcom.2017.04.053.

Supplementary Material

The following online material is available for this article:

Figure S1 - XRD patterns of the Mg–Y–Gd–Zr alloy in the as-cast, solution heat-treated (525 °C/24 h), and aged (100 h and 200 h) conditions.

Figure S2 - Thermodynamic prediction of phase evolution during solidification of the Mg–Y–Gd–Zr alloy obtained by Thermo-Calc® using the Scheil–Gulliver approach.